Research Article

Improving treatment for Parkinson's disease: Harnessing photothermal and phagocytosis-driven delivery of levodopa nanocarriers across the blood-brain barrier

Kaili Liang, Li Yang, Jiawei Kang, Bo Liu, Ding Zhang, Liyan Wang, Wei Wang, Qing Wang*

State Key Laboratory of Fine Chemicals, Department of Pharmaceutical Engineering, School of Chemical Engineering, Dalian University of Technology, Dalian 116024, China

ARTICLE INFO

ABSTRACT

Parkinson's disease (PD) poses a significant therapeutic challenge, mainly due to the limited ability of drugs to cross the blood-brain barrier (BBB) without undergoing metabolic transformations. Levodopa, a key component of dopamine replacement therapy, effectively enhances dopaminergic activity. However, it encounters obstacles from peripheral decarboxylase, hindering its passage through the BBB. Furthermore, levodopa metabolism generates reactive oxygen species (ROS), exacerbating neuronal damage. Systemic pulsatile dosing further disrupts natural physiological buffering mechanisms. In this investigation, we devised a ROS-responsive levodopa prodrug system capable of releasing the drug and reducing ROS levels in the central nervous system. The prodrug was incorporated within second near-infrared region (NIR-II) gold nanorods (AuNRs) and utilized angiopep-2 (ANG) for targeted delivery across the BBB. The processes of tight junction opening and endocytosis facilitated improved levodopa transport. ROS scavenging helped alleviate neuronal oxidative stress, leading to enhanced behavioral outcomes and reduced oxidative stress levels in a mouse model of PD. Following treatment, the PD mouse model exhibited enhanced flexibility, balance, and spontaneous exploratory activity. This approach successfully alleviated the motor impairments associated with the disease model. Consequently, our strategy, utilizing NIR-II AuNRs and ANG-mediated BBB penetration, coupled with the responsive release of levodopa, offers a promising approach for dopamine supplementation and microenvironmental regulation. This system holds substantial potential as an efficient platform for delivering neuroprotective drugs and advancing PD therapy.

* Corresponding author.
E-mail address: qwang@dlut.edu.cn (Q. Wang).
Peer review under responsibility of Shenyang Pharmaceutical University.

1. Introduction

Parkinson's disease (PD) poses a formidable challenge in the field of neurology [1,2], characterized by severe and progressive neurodegeneration involving the pathological loss of dopaminergic neurons in the substantia nigra and subsequent impairment of neuronal mitochondrial function [3]. The etiology of dopaminergic neuron loss is attributed to oxidative stress, resulting from elevated dopamine turnover, insufficient glutathione (GSH) levels, and increased levels of reactive oxygen species (ROS) within the substantia nigra [4]. In treating PD, the blood-brain barrier (BBB) is critical and highly selective [5], significantly restricting drug permeation into the brain [6,7]. This limitation severely hampers drug penetration [8] and presents a challenge for delivering targeted doses into the brain without undesired metabolic transformations [9]. Addressing these complexities would greatly benefit therapeutic strategies for PD.

Levodopa (LD) is commonly used in the treatment of PD. However, its therapeutic efficacy is hindered by peripheral decarboxylase, which converts it into dopamine, a crucial molecule needed in the corpus striatum of PD patients, but faces challenges in crossing the BBB [10]. To enhance LD's ability to penetrate the brain, it is often co-administered with peripheral decarboxylase inhibitors like benserazide or carbidopa to reduce peripheral LD metabolism and increase BBB permeability [11]. However, this drug delivery system primarily improves patients' behavioral symptoms while unintentionally exacerbating neuronal damage due to the increased influx of pro-oxidant LD [12]. LD induces damage to neuronal cells through two primary mechanisms. Firstly, LD and dopamine generate ROS during their metabolic and autoxidation processes, leading to oxidative damage [13]. Secondly, LD disrupts thiol homeostasis, resulting in the loss of various antioxidant enzymes such as glutaredoxin (Grx) and superoxide dismutase (SOD) [14], impairing the body's redox regulation capacity and exacerbating oxidative stress. Recognizing the role of LD metabolism in generating ROS can guide the development of more effective treatment strategies to reduce ROS-induced oxidative stress in neurons. This understanding is crucial for addressing the potential side effects of LD therapy in PD. Additionally, prolonged use of the LD-carbidopa delivery system may introduce side effects related to diminishing the body's buffering capacity, necessitating dose escalation with disease progression [15]. Therefore, it is crucial to explore approaches that facilitate the passage of LD across the BBB with reduced side effects and alleviate central nervous system oxidative stress in Parkinson's patients.

In this study, we have developed a nanocarrier, Au-PCBLD-ANG, designed to deliver LD across the BBB and release it in response to reactive ROS (Fig. 1B). The core of this drug delivery system comprises gold nanorods (AuNRs) [16] in the second near-infrared region (NIR-II), known for their excellent tissue penetration and photothermal conversion efficiency, thereby enhancing BBB permeability. To safeguard LD from degradation by peripheral decarboxylase enzymes, we devised a drug-loaded polymer, PCB-Se-Se-LD (PCBLD), linked by ROS-labile diselenide bonds (-Se-Se-), and encapsulated it around

the AuNR. The outermost layer of this drug delivery system is angiopep-2 (ANG, TFFYGGSRGKRNFKTEEY) [17], which can bind to low-density lipoprotein receptor-related protein 1 (LRP1) in the BBB. This facilitates targeted drug delivery and transcytosis mediated by LRP1 to enter the brain [18].

The process and mechanism of this nanocarrier delivery are illustrated in Fig. 1C. In the bloodstream, nanoparticles accumulate in the BBB region, which expresses high levels of LRP1 through ANG targeting. They are transcytosed into the brain. Simultaneously, NIR-II laser irradiation induces photothermal conversion, increasing BBB permeability through the AuNRs. The synergistic effect of photothermal conversion and cellular uptake significantly boots the transport of LD into the brain. Once the nanoparticles enter the brain, the diselenide bonds break due to the elevated ROS levels in the brains of Parkinson's patients, causing the breakdown of the drug-loaded polymer and the release of LD. Subsequently, the drug-loaded polymer is degraded to release LD in its selenic acid form. Esterase enzymes then hydrolyze LD selenic acid into LD, which is further converted into dopamine by decarboxylases, achieving dopamine supplementation in the brains of Parkinson's patients. In this delivery process, the oxidative cleavage of diselenide bonds significantly reduces ROS levels in the patient's brain, effectively lowering oxidative damage and enhancing the balance of the brain's microenvironment. This strategy effectively interrupts the harmful cycle of elevated ROS levels, impaired mitochondrial function, and decreased reductase activity in the central nervous system, thereby reducing oxidative damage and improving the brain's microenvironment for patients. By harnessing photothermal effects and phagocytosis, this approach overcomes the challenge of LD crossing the BBB and counteracts the worsening of oxidative damage and neuronal injury associated with LD administration by reducing ROS levels in the central nervous system. This innovative method combines the phagocytic properties of ANG and the photothermal capabilities of NIR-II AuNR to achieve efficient, targeted delivery of LD across the BBB, resulting in successful drug delivery. Moreover, it modulates the brain microenvironment to reduce neuronal damage by lowering ROS levels. This approach more effectively addresses the underlying causes of Parkinson's disease, such as oxidative stress and mitochondrial dysfunction, offering a new promising avenue for potentially slowing disease progression and improving the quality of life for patients.

2. Materials and methods

2.1. Materials

Sodium borohydride (NaBH$_4$), cetyltrimethyl ammonium bromide (CTAB), hydroquinone, ascorbic acid, silver nitrate (AgNO$_3$), gold (III) chloride hydrate (HAuCl$_4$), 1-methyl-4-phenylpyridinium ion (MPP$^+$), 1-methyl-4-phenyl-1,2,3,6-tetrahydropyridine (MPTP), and rabbit polyclonal anti-TH antibody were purchased from SigmaAldrich (MO, USA). LD, 9-Fluorenylmethyl chloroformate (Fmoc-Cl), tert-butyldimethylsilyl chloride (TBS-Cl), Se powder,
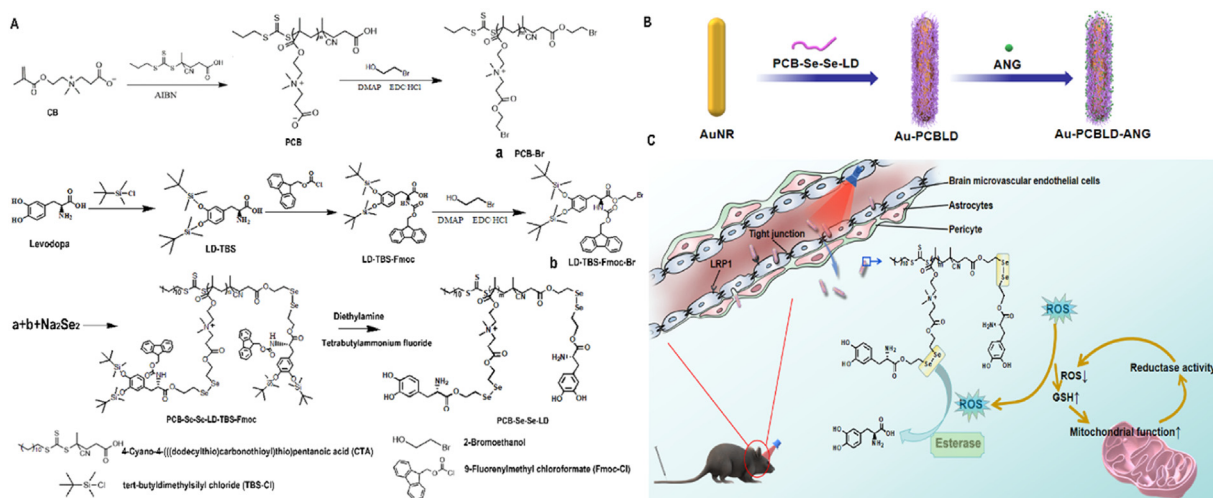
Fig. 1 – Schematic of the preparation and therapeutic mechanism of Au-PCBLD-ANG. (A) Synthesis pathway of PCB-Se-Se-LD. (B) Layer-by-layer assembly of AuNR, PCB-Se-Se-LD, and ANG through electrostatic adsorption to form Au-PCBLD-ANG NPs. (C) Targeting of the BBB by Au-PCBLD-ANG, traversing the BBB through the dual mechanisms of photothermal effects and phagocytosis. Upon reaching the brain, the -Se-Se- bonds of PCBLD undergo oxidation in the presence of elevated ROS concentration. This oxidation leads to the subsequent release of LD in the presence of brain esterases. LD can further be metabolized into DA by decarboxylases, thus supplementing DA in the central nervous system of Parkinson's patients. A substantial amount of ROS is consumed throughout this process, interrupting the detrimental cycle involving high ROS levels, mitochondrial dysfunction, and neuronal damage.

sodium borohydride, 2,2′-dicyano-2,2′-azopropane (AIBN), carboxybetaine (CB), 4-cyano-4-(((dodecylthio)carbonothioyl)thio)pentanoic acid (CTA), 1,8-diazabicyclo [5.4.0]undec-7-ene (DBU), 4-dimethylaminopyridine (DMAP) and 1-(3-dimethylaminopropyl)-3-ethylcarbodiimide hydrochloride (EDC·HCl) (purity ≥99%) were purchased from Aladdin Reagent Co., Ltd. (Shanghai, China). The Cell Counting Kit-8 (CCK-8) and ELISA test kits were purchased from Solarbio Laboratories (Beijing, China). All other chemicals were unmodified prior to use and were of analytical grade.

2.2. Preparation of Au-PCBLD-ANG

In this study, we synthesized poly(carboxybetaine) (PCB) using reversible addition-fragmentation chain transfer (RAFT) polymerization [19]. Initially, we dissolved CB (1.00 g, 4.35 mmol), CTA (176.00 mg, 0.44 mmol), and AIBN (29.35 mg, 0.18 mmol) in 5 ml anhydrous methanol. The solution was then subjected to freezing, degassing, and thawing, followed by a 24-h reaction at 65 °C. Subsequently, we dialyzed and freeze-dried the resulting product for future use. Next, we dissolved the synthesized PCB (100.00 mg, 0.03 mmol), DMAP (63.95 mg, 0.52 mmol), and EDC·HCl (120.45 mg, 0.63 mmol) in DMSO. We added 2-bromoethanol (54.5 mg, 31 µl) dropwise to the solution, and the mixture was stirred at room temperature for 48 h. The final product, PCB-Br, was obtained through dialysis and freeze-drying.

To protect the LD molecule from potential impacts during subsequent synthesis steps, we used TBS-Cl and Fmoc-Cl to shield its hydroxyl and amino groups, preparing LD-TBS-Fmoc. TBS-Cl (2.08 g, 13.83 mmol) was dissolved in acetonitrile (10 ml), and LD (0.91 g, 4.60 mmol) was

added while cooling on ice. DBU (2.08 ml, 13.80 mmol) was introduced, and the mixture was stirred for 4 h in an ice bath, followed by a 20-h reaction at room temperature. Cold (−20 °C) acetonitrile was added to the reaction, and the crude product was obtained by filtration through a silica gel column. The resulting solid (3.60 g, 8.43 mmol) was combined with diethyl ether (50 ml) and a 10 % Na_2CO_3 solution, followed by stirring for 10 min. Fmoc-Cl (2.18 g, 8.43 mmol) was then added, and the reaction proceeded for 4 h on ice and 18 h at room temperature. After extraction and purification, LD-TBS-Fmoc was obtained. LD-TBS-Fmoc (2.30 g, 3.55 mmol) was dissolved and mixed with DMAP (0.64 g, 5.20 mmol) and EDC·HCl (1.20 g, 6.30 mmol). After complete dissolution, 2-bromoethanol (0.55 g, 310.00 µl) was added dropwise to the solution, followed by stirring at room temperature for 48 h. The product was extracted and purified, resulting in TBS-Fmoc-LD-Br. Structural characterization was performed through nuclear magnetic resonance (NMR) spectroscopy.

For the synthesis of PCBLD prodrugs, PCB-Br (70.6 mg, 0.02 mmol) and TBS-Fmoc-LD-Br (110.0 mg, 0.14 mmol) were dissolved in DMSO. A solution of Na_2Se_2 (89.7 mg, 0.57 mmol) was added under nitrogen protection with magnetic stirring, and the mixture was stirred at 50 °C for 24 h. The product was then dialyzed and freeze-dried, resulting in PCB-Se-Se-TBS-Fmoc-LD. According to previous studies, the Fmoc protecting group was removed with diethylamine, while the TBS protecting group was removed using tetrabutylammonium fluoride [20]. The final product, PCBLD, was obtained and its structure was characterized through NMR spectroscopy. The polymer molecular weights were analyzed by gel permeation chromatography (GPC), using water as the solvent.

To fabricate Au-PCBLD-ANG, surface-charged AuNR with an aspect ratio of 6.7 were synthesized through seed-mediated growth using hydroquinone as a seed [21]. The synthesis AuNR using a hydroquinone seed-mediated growth approach involves the following steps: First, heat 5 ml of a 0.001 M HAuCl$_4$ solution to boiling, and rapidly introduce 5 ml CTAB while vigorously stirring. Subsequently, stir the mixture on a hotplate at 1,200 rpm for 30 s. After allowing it to rest for a few min, combine the seed solution with the growth solution, which consists of 75 µl of 100 mM AgNO$_3$ (aq). Next, gently mix in 500 µl of a 0.1 M hydroquinone aqueous solution. Over time, the solution will transform from an orange hue to a clear, pale yellow turbid appearance. Finally, introduce 15 µl the seed solution into the growth mixture and incubate it for 12 h, followed by two centrifugation steps at 8,000 $\times g$, each lasting 30 min. The nanorods are dissolved in the sodium citrate solution and, after centrifugation, dispersed in water. Subsequently, a layer-by-layer coating method was employed. The prepared AuNR were centrifuged to remove the supernatant, and then they were mixed with a solution of PCB-Se-Se-LD (5.00 mg/ml) dissolved in 1 mM NaCl aqueous solution. After a 30-min adsorption period, excess polymer was removed by centrifugation at 8,000 rpm for 6 min, and the precipitate was further dispersed in NaCl aqueous solution. This solution was added to ANG protein (1.00 mg) freeze-dried powder and adsorbed for 30 min, followed by centrifugation and dispersion of the precipitate in deionized water. During the preparation of gold nanorods, we adjust the concentration of AgNO$_3$ to achieve the desired aspect ratio. In the assembly of nanoparticles, selecting the correct concentration of NaCl solution for electrostatic adsorption experiments involving polymers on gold nanorods is crucial for successful assembly. Electrostatic adsorption depends on the charge interactions between the polymers and the gold nanorods. NaCl helps shield these interactions by compressing the double layer around the charged entities. By fine-tuning the NaCl concentration, we ensure successful polymer coverage on the surface of the gold nanorods.

2.3. Characterization of Au-PCBLD-ANG

Nanoparticle (NP) size and ζ-potential are determined through dynamic light scattering (DLS) measurements. The final size and morphology of NPs were observed using a transmission electron microscope (TEM) operated at an acceleration voltage of 200 kV (JEM-2100 electron microscope). The drug loading (DL) amount was detected using a UV–Vis-NIR spectrophotometer. The presence of Se elements in the NP solution was verified via inductively coupled plasma mass spectrometry (ICP-MS). The following formulas were used to calculate the LD's loading efficiency (EE) and DL of the NPs:

$$EE\ (\%) = \frac{\text{weight of LD in Au} - \text{PCBLD} - \text{ANG}}{\text{initial weight of LD}} \times 100\%$$

$$DL\ (\%) = \frac{\text{weight of LD in Au} - \text{PCBLD} - \text{ANG}}{\text{weight of Au} - \text{PCBLD} - \text{ANG}} \times 100\%$$

To evaluate the photothermal conversion efficiency of the NPs, we subjected them to irradiation under a 1064 nm NIR laser (provided by China Changchun New Industrial

Technology Co., Ltd.) with a power density of 0.8 W/cm^2. Subsequently, we monitored the temperature of these solutions at 30-s intervals during the irradiation using an infrared thermal imaging system. The calculation of photothermal conversion efficiency is as follows:

$$\eta = \frac{hS(T_{max} - T_{surr}) - Q_0}{I\left(1 - 10^{-A_\lambda}\right)}$$

Where h is the heat transfer coefficient, S is the container surface area, T_{max} and T_{surr} are the equilibrium and ambient temperatures, respectively, Q_0 is the heat associated with the light absorbance of the solvent, A_λ is the absorbance of Au-PCBLD-ANG at 1064 nm, and I is the laser power density.

2.4. In vitro release of LD

Au-PCBLD-ANG encapsulated in a dialysis bag with a molecular weight cutoff of 3,500 Daltons was incubated in 100 ml PBS at 37 °C under horizontal agitation, with or without the addition of 0.01 % H$_2$O$_2$. At predefined time intervals, the solution was withdrawn and replaced with an equal volume of fresh solution. Prior to analysis, the samples were treated with esterase (10 U) for 24 h. The concentration of LD was determined using an HPLC method. We calculated the cumulative release amount of LD at each time point and analyzed the cumulative release rates for each group within a 24-h period. The cumulative release of LD was calculated using the following formula:

$$\text{Release ratio (\%)} = \frac{W_1}{W_2} \times 100\%$$

Where W_1 represents the weight of LD in the solution, and W_2 represents the total weight of LD in the NPs.

2.5. Cell culture and experimental animals

Cultured immortalized mouse brain-derived endothelial cells (bEnd.3), astrocytes (AC) and human neuroblastoma cell lines (SH-SY5Y) were procured from the North Biological Technology Research Institute in Beijing, China. These cells were maintained in DMEM-H supplemented with 10 % fetal bovine serum (FBS) at 37 °C with 5 % CO$_2$ in a cell culture incubator.

For animal experiments, 8-week-old C57BL/6 mice were obtained from Changsheng Biotechnology Co., Ltd. in Changchun, China. The animals were housed in a standard facility maintained at 25 ± 2 °C with a relative humidity of 55 % ± 5 %, under a 12-h light-dark cycle, and provided with ample food and water. All animal studies were performed in accordance with the Dalian University of Technology guidelines for the welfare of experimental animals (Approval number: DUTSCE220813_01).

2.6. Transwell model for in vitro BBB permeability

The BBB mainly consists of capillary endothelial cells, with AC cell enhancing its formation through interactions with these

cells. We constructed an *in vitro* transwell BBB model using both bEnd.3 and AC cells. In this experiment, we established an *in vitro* BBB model system based on previous studies [22,23]. In brief, to enhance cell adhesion, the lower chamber of Transwell filters (12 mm diameter, 0.4 µm pore size, 1.12 cm² growth area) was treated with collagen type I (8 µg/cm² in 0.02 N acetic acid) for 1 h at room temperature, followed by a PBS wash. Subsequently, AC cells (2.5×10^4 cells/cm²) were seeded on the lower membrane for 3 h, and bEnd.3 cells (1×10^5 cells/cm²) were added to the upper membrane. The cells were co-cultured for 4 d, and samples with a trans-epithelial electrical resistance (TEER) greater than 200 Ω·cm² were used for BBB permeability measurements. Since peripheral decarboxylases primarily influence the LD drug during administration in this study, we introduced decarboxylase and coenzyme vitamin B6 into the Transwell model to simulate the BBB model system comprehensively. We assessed the effectiveness of each method in assisting drug passage to cross the BBB model using 600 µg LD or NPs containing an equivalent dose of LD.

We introduced each type of NP into the upper chamber and collected solutions from the lower chamber at different intervals. Subsequently, these solutions were reacted with sufficient H_2O_2, enabling us to measure the cumulative transmittance of LD in each group.

2.7. In vitro neuroprotection

For assessing cell viability, bEnd.3, AC and SH-SY5Y cells were seeded in 96-well plates (5×10^3 cells/well) and incubated for 24 h. Subsequently, a series of concentrations of Au-PCBLD-ANG (0–200 µg/ml or 0–20 µM) were used to treat the cells for 12 h. Following treatment, an appropriate volume of CCK-8 solution was added to each well, and the plate was further incubated for 4 h. Cell viability was measured using a CCK-8 assay kit, and the absorbance at 450 nm was determined using a microplate reader (Emax Precision, USA).

For the detection of ROS, DCFH-DA was diluted 1:1,000 in serum-free culture medium to achieve a final concentration of 10 µM. The culture medium was removed, and the appropriately diluted DCFH-DA was added to the cells. After incubation at 37 °C for 20 min in a cell culture incubator, the cells were washed three times with serum-free culture medium to remove any DCFH-DA that had not entered the cells. After 30 min, the absorbance at 488 nm was measured using a microplate reader. The measurement of GSH, ATP, and mitochondrial membrane potential (JC-1) was also conducted using similar methods, and the ATP, ROS and JC-1 assay kits were purchased from Solarbio.

2.8. NPs entry into bEnd.3 cells by fluorescence imaging

We cultured bEnd.3 cells in a confocal dish for 3 d to prepare a BBB planar model. For cell imaging, different NPs labeled with Cy3.5 were used to treat the cells for 30 min. The cells were washed to remove NPs that did not enter them. Cell fixation was carried out using 4 % neutral formaldehyde solution at 4 °C for 15 min. Subsequently, the cell nuclei were stained with DAPI dye. Imaging was performed using a confocal fluorescence microscope.

2.9. Biocompatibility assay

To assess serum stability, Au-PCBLD-ANG NPs were suspended in PBS, 10 %, 20 % or 50 % FBS and their LD concentration was measured at room temperature over 0–24 h using an HPLC system.

In vitro hemolytic toxicity of Au-PCBLD-ANG formulation was evaluated using red blood cells (RBCs) isolated from rabbit heart blood, stabilized with EDTA (0.2 ml) in a 5 ml volume. These RBCs were separated by centrifugation, washed in 2 % PBS, and then mixed with 500 µl RBCs and 500 µl Au-PCBLD-ANG in PBS (at concentrations of 50, 100 or 200 µg/ml LD). Additionally, PBS and water were used as negative and positive controls, respectively. After incubating at room temperature for 3 h, the samples were centrifuged, and the absorbance of the supernatant at 570 nm was measured using UV–Vis-NIR spectrophotometer.

2.10. Pharmacokinetics studies

Pharmacokinetic studies of blood and brain were conducted in randomly assigned groups of male C57BL/6 mice, which were treated as follows: (i) LD, (ii) Au-PCB+NIR-II irradiation, (iii) Au-PCBLD-ANG, (iv) Au-PCBLD-ANG+NIR-II irradiation. All animals received the appropriate compounds intravenously at an LD equivalent dose of 60/mg kg and were then subjected to laser irradiation at 1064 nm (0.8 W/cm², 41 ± 1 °C, 10 min) in the irradiation group. Blood was collected from the mice within 0–24 h post-treatment. We collected 50 µl venous blood from mice using the method of venipuncture from the medial canthus vein. The blood was immediately transferred to a tube containing sodium heparin as an anticoagulant. To precipitate proteins, 150 µl methanol was added to the sample, followed by vigorous oscillation for 5 min. Subsequently, the mixture was centrifuged at 12,000 rpm for 10 min at 4 °C. We then collected 60 µl the supernatant for further analysis. The brain tissue homogenate was prepared after blood collection and systemic blood clearance by perfusion. The LD levels in these samples were quantified using HPLC.

2.11. Evans Blue dye quantification

Evans Blue, a dye frequently utilized to investigate the permeability of the BBB, is administered intravenously to animals and permeates brain tissue via the BBB [24]. Consequently, we employed Evans Blue as a tracer to assess the capability of each group to open the BBB. Following treatments with NIR-II, NIR-II+PCBLD, NIR-III+Au PCBLD, or NIR-II+Au PCBLD ANG, mice received an intravenous injection of a 2 % Evans Blue solution (dosed at 4 mg per kg of mice weight). 30 min later, a cardiac perfusion procedure was carried out. The anesthetized mice were positioned in a supine manner, and the chest was opened to expose the heart. A needle was swiftly inserted along the axis of the heart into the left ventricle. Once blood reflux ceased, hemostatic forceps clamped and secured the needle tip puncture. The

right atrium was then incised, leading to a significant blood volume of Evans Blue dye outflow. The heart underwent perfusion with physiological saline, and after approximately 10 ml of perfusion, the effluent from the right atrium became clear. The perfusion continued for an additional 40 ml before the brain was harvested. Brain tissues were weighed and homogenized in a 50 % pre-cooled trichloroacetic acid solution at a ratio of 1.5 ml/g. After centrifugation at 3,000 rpm/min for 20 min, the supernatant was subjected to analysis for absorbance at 620 nm using an enzyme-linked immunosorbent assay (ELISA). Evans Blue content in each homogenate was determined based on a standard curve, indicating blood-brain barrier permeability.

2.12. Lanthanum nitrate tracing

Lanthanum nitrate is a tracer extensively utilized in biomedical research, particularly for studies investigating the mechanisms of BBB opening. Upon injection into the body, it enters the bloodstream and is transported to the cerebral vascular system. Normally, the presence of the BBB prevents lanthanum nitrate from crossing into brain tissue. However, when the barrier is compromised, lanthanum nitrate can penetrate the vascular wall and accumulate, facilitating observation via TEM [25]. Consequently, lanthanum nitrate tracing is used to assess the condition of the BBB after therapeutic interventions.

Following the treatment, each experimental group of mice underwent anesthesia, and a swift chest opening allowed for the insertion of a cannula into the left ventricle. Heparinized physiological saline was perfused to purify the blood, succeeded by the infusion of 200 ml lanthanum nitrate fixative solution, maintaining a perfusion pressure of 16 kPa (120 mm Hg). After 25–30 min of perfusion, the skull was opened, and the right cerebral tissue was promptly excised. This tissue was immediately immersed in lanthanum nitrate fixative solution, trimmed into 1 mm tissue blocks, and further fixed for over 2 h. Subsequently, the tissue blocks were rinsed in a 0.1 mol/l dimethyl arsenate sodium buffer containing lanthanum, repeated three times for approximately 10 min each. Following this, they were fixed in a 1 % osmium tetroxide solution without lanthanum for 2 h. The tissue blocks were then washed with dimethyl arsenate sodium buffer, gradually dehydrated in ethanol and acetone, embedded in Epon 812 resin, sectioned into ultrathin slices, uranium stained, lead stained for 10 s, and finally observed under a TEM.

2.13. Tight junction and adherens junction protein detection

The levels of ZO-1, occludin, and VCAM proteins in mouse brain homogenates before and after treatment were evaluated using the ELISA technique. Brain samples were collected briefly before treatment and at 0, 12 and 24 h post-treatment, followed by homogenization. Taking ZO-1 as an example, 10 μl test samples from each group were loaded into sample wells, and then 40 μl sample diluent was added. Subsequently, 100 μl detection antibody labeled with horseradish peroxidase (HRP) was introduced into each well, and the mixture underwent incubation at 37 °C for 60 min. After discarding the liquid, the wells were washed. Following this, 50 μl substrate A and B were added to each well, and the plate was incubated in the dark at 37 °C for 15 min. Finally, 50 μl stop solution was added to each well, and each well's optical density (OD) was measured at a wavelength of 450 nm within 15 min.

2.14. Establishment of the PD model and drug administration

The PD model of C57BL/6 mice was established via intraperitoneal injections of MPTP. Given the individual differences among the animals and variations in dosages, the MPTP-induced PD model may display inherent variability, which could influence the analysis of subsequent experimental outcomes. To mitigate this, we meticulously controlled the administered dosage, tailoring it to the body weight of each mouse to ensure consistency and reliability in our results. The mice were administered MPTP intraperitoneally at a dosage of 18 mg kg^{-1} four times a d with 2-h intervals between injections, whereas control mice were administered equivalent doses of normal saline [26]. After MPTP treatment, the animals received treatments with LD, LD/benserazide hydrochloride (LBH), Au-PCB-ANG, NIR-II+Au-PCB, and NIR-II+Au-PCB-ANG, respectively. The irradiated group of mice was exposed to a 1064 nm laser (0.8 W/cm^2, 41 ± 1 °C) for 10 min.

In our mouse treatment protocol, dosing is determined based on body weight, with 60 mg LD administered per kg of mouse body weight. Based on the drug loading capacity, calculate and inject NPs containing an equivalent dose of LD.

The rotarod, pole climbing, and open field tests are routinely utilized for behavioral assessments in animal models of PD. Individual variability may influence the outcomes of these assessments. To mitigate this, we implemented environmental adaptation and behavioral training for the mice before beginning the treatment.

2.14.1. Behavioral experiment with animals
Rotarod test: It involves exposing mice to a rotating rod with a 7 cm diameter, set at a fixed speed of 20 rpm/min for 2 min. The measurement included the time each mouse spent on the rod (fall latency) and the total duration of falls.

Pole-climbing test: In this test, mice were placed head down on a vertically positioned rough-surfaced pole with a 1 cm diameter and a height of 50 cm. Each mouse was initially positioned head up near the top of the pole, and the recorded parameters included the time taken to turn (T-Turn) and the time taken to reach the bottom (T-Total).

Open field test: The open field test was conducted in a defined area (50 cm × 50 cm × 40 cm) where each mouse was placed in the center and allowed to explore freely for 5 min. The total distance moved, and average moving speed was then recorded during a 5-min test.

Anesthesia may affect the behavior and biochemical markers of animals. In our study, the behavior of mice returned to normal within 10–30 min after mild anesthesia. Therefore, we assessed both mouse behavior and biochemical markers at least 30 min after anesthesia to ensure the reliability of our observations.

2.15. Immunostaining of brain tissue

Following a previously established protocol, immunofluorescence analysis was conducted to quantify the number of tyrosine hydroxylase positive (TH$^+$) neurons in the central nervous system. Mouse brains underwent fixation in 4 % paraformaldehyde and subsequent dehydration in 30 % sucrose. Following dehydration, the brains were sectioned into slices of 30 µm thickness and incubated in 10 % goat serum for 30 min. Subsequently, the slices were incubated overnight at 4 °C to an anti-TH$^+$ antibody (dilution 1:2,000). After three washes with PBS, the slices were subjected to a 2 h incubation at room temperature with secondary antibodies coupled with Alexafluor 594. Following DAPI staining, the slices were observed under a fluorescence microscope.

2.16. Statistical analysis

Data are means ± SD and were compared via one- and two-way analyses of variance (ANOVAs) as appropriate. $P < 0.05$ was the significance threshold.

3. Results and discussion

3.1. Preparation and characterisation of Au-PCBLD-ANG NPs

The synthesis of PCB with a consistent molecular weight (MW) of 3.53 kDa involved RAFT [19] (Figs. 1 and S2). To protect the LD molecule from potential impacts during subsequent synthesis steps, we employed TBS-Cl and Fmoc-Cl to protect its hydroxyl and amino groups. This led to the formation of LD-TBS-Fmoc. Subsequently, PCB-LD-TBS-Fmoc was prepared by connecting PCB and LD-TBS-Fmoc using Na_2Se_2 and deprotection to yield PCBLD (15.82 kDa) (Fig. S2). We confirmed the successful synthesis of PCB, PCB-Br, LD-TBS-Fmoc, PCB-Se-Se-LD-TBS-Fmoc, PCB-Se-Se-LD, and PCB-Cy3.5 through ^{1}H NMR (Fig. S1). Since the diselenide bond is the crucial component of our design for scavenging ROS, we measured the selenium content. Using ICP-MS (Fig. S3), we observed a characteristic absorption peak at 196.025 nm, indicating a selenium concentration of 120.35 µg/mg in the polymer. GPC confirmed molecular weights of 3.53 kDa for PCB and 15.82 kDa for PCB-LD (Fig. S2).

NIR-II aspect ratio 6.7 surface-exposed carboxylated AuNRs were prepared using a seed-mediated method [21]. Analysis through TEM and UV-IR-VS determined the size of these AuNRs to be approximately 16 nm × 107 nm (Fig. 2A), with an absorption wavelength of 1090 nm (Fig. 2B). AuNRs of this wavelength possess deep tissue penetration and are suitable for biological environments [27,28]. In this study, NPs were synthesized using a layer-by-layer coating approach through electrostatic adsorption. By covering the surface with negatively charged gold nanorods coated with sodium citrate and adsorbing positively charged polymers, we evaluated the surface charge of the gold nanorods, which measured −36.53 ± 1.99 mV (Fig. 2C). This indicates the successful attainment of a negative charge on the NPs surfaces. Subsequently, Au, PCBLD, and ANG were assembled into Au-PCBLD-ANG nanocarriers using a layer-by-layer coating method and characterized by TEM, UV-IR-VS, and zeta potential. TEM revealed that the prepared Au-PCBLD-ANG had dimensions of approximately 25 nm × 113 nm (Fig. 2A). The polydispersity index (PDI) of the NPs was determined to be 0.21 ± 0.03 using DLS detection (Table S1). This suggested that the prepared NPs exhibit a uniform size distribution. UV-IR-VS analysis showed maximum absorption at 1064, making it suitable for NIR-II laser irradiation (Fig. 2B). The surface charges of Au, Au-PCB and Au-PCBLD-ANG were −36.53 ± 1.99, 33.83 ± 0.49 and 3.04 ± 0.81 mV, respectively (Fig. 2C). AuNRs with negatively charged, exposed carboxyl groups on their surface showed a positive surface charge after being coated with positively charged PCBLD. When the negatively charged ANG adsorbs to the polymer surface, the NPs exhibit an overall neutral charge. Based on UV-IR-VS analysis of the coating content, we achieved EE and DL of approximately 83.63% and 16.76%, respectively.

3.2. Assessment of NIR-II laser-induced photothermal efficacy and drug release

Subsequently, we subjected the Au-PCBLD-ANG solution to continuous exposure to a 1064 nm laser (0.8 W/cm^2) to investigate the photothermal efficacy of the Au-PCBLD-ANG formulation against radiation. The highest observed heating temperature allowed us to calculate a photothermal conversion efficiency (η) of 26.10 % ± 0.63 % (Fig. 2D). Furthermore, the absorption spectrum of NRs remained unchanged after NIR-II exposure, indicating that NRs did not degrade during the temperature elevation induced by laser irradiation (Fig. S4).

LD was released using ROS-induced disulfide bond cleavage to facilitate the release of LD from the NPs. The disulfide bonds underwent facile oxidation to selenic acid, subsequently liberating LD as a free form upon exposure to esterase treatment [29]. As illustrated in Fig. 2E, when subjected to esterase at 37 °C in PBS without H_2O_2 and laser irradiation, LD remained undetectable during the 0–16 h incubation period. A small amount (0.41 % ± 0.17 %) of LD was released at 24 h, possibly due to slow oxidation and release in the presence of atmospheric oxygen. In the absence of H_2O_2, NIR-II within the NP system resulted in a 2.73 % ± 0.28 % release of LD. This occurred because the photothermal process of gold NPs generated a small amount of ROS, causing the oxidation of diselenide bonds in PCB and the subsequent limited release of LD. In contrast, the groups with the addition of 0.01 % H_2O_2, namely, H_2O_2+Au-PCBLD-ANG and H_2O_2+NIR-II+Au-PCBLD-ANG, exhibited a substantial release of LD. After 12 h of incubation, release was nearly complete, accumulating 71.43 % ± 2.60 % and 87.72 % ± 2.61 %, respectively, by the 24-h mark. The group subjected to laser irradiation demonstrated an accelerated release rate and higher LD release. This outcome is likely attributable to the elevated temperature expediting the reaction rate and the photothermal process of AuNRs generating additional ROS, thereby augmenting the overall release. When co-incubated with H_2O_2, the release rates of H_2O_2+NIR-II+Au-PCBLD-ANG and H_2O_2+Au-PCBLD-ANG were 214.7 ± 3.69 times and 174.9 ± 2.48 times, respectively, those of
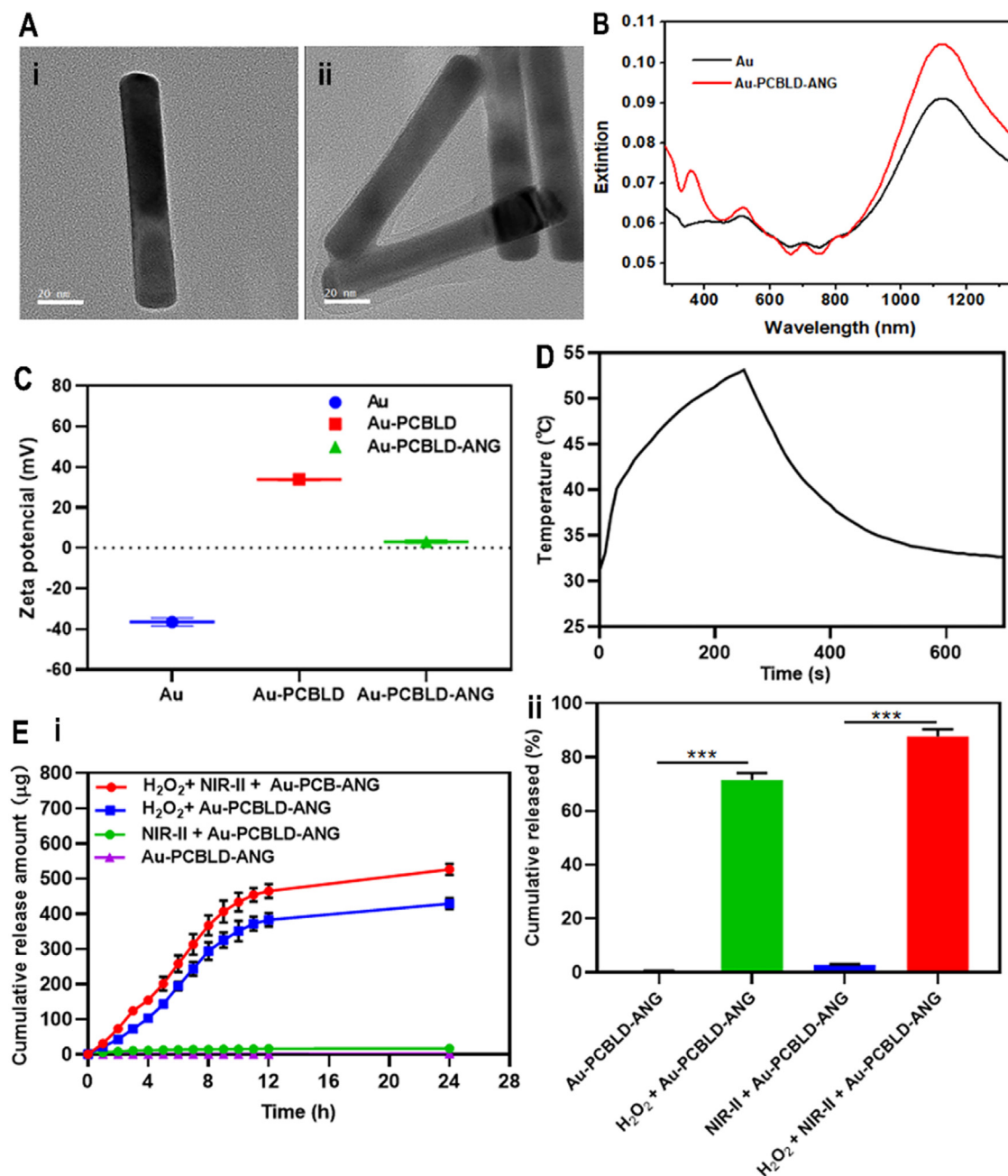
Fig. 2 – Characterization of nanocarriers. (A) TEM images of (i) AuNR (scale bar: 20 nm) and (ii) Au-PCBLD-ANG (scale bar: 20 nm). (B) Absorption spectra of AuNR and Au-PCBLD-ANG. (C) Zeta potential measured by DLS technique. (D) Temperature profile of Au-PCBLD-ANG solution (50 μg/ml of LD) following 1064 nm laser irradiation and cooling after irradiation termination. (E) (i) Cumulative release profiles of LD from NPs over time, with or without H_2O_2. (ii) Accumulated LD release in each group over 24 h; $n = 3$. **$P < 0.01$, ***$P < 0.001$.

NIR-II+Au-PCBLD-ANG and Au-PCBLD-ANG without H_2O_2. The presence of H_2O_2 significantly increased LD release, indicating that the formulated drug-loaded NPs can efficiently release LD through oxidation.

3.3. Evaluation of permeability in an in vitro BBB model

The BBB predominantly comprises endothelial (bEnd.3) cells lining brain capillaries, and their interactions with other cell types collectively maintain BBB functionality [22]. AC are among the most abundant non-neuronal cell types in the brain and contribute to BBB formation through interactions with bEnd.3 cells [23]. In this investigation, we established an *in vitro* BBB model using bEnd.3 cells and AC cells on Transwell inserts (Fig. 3A) to explore the capability of drug delivery systems to transport drugs across the BBB [30]. The TEER of the BBB model consistently exceeded 200 ohms/cm^2 (Fig. 3B), confirming the successful construction of the BBB
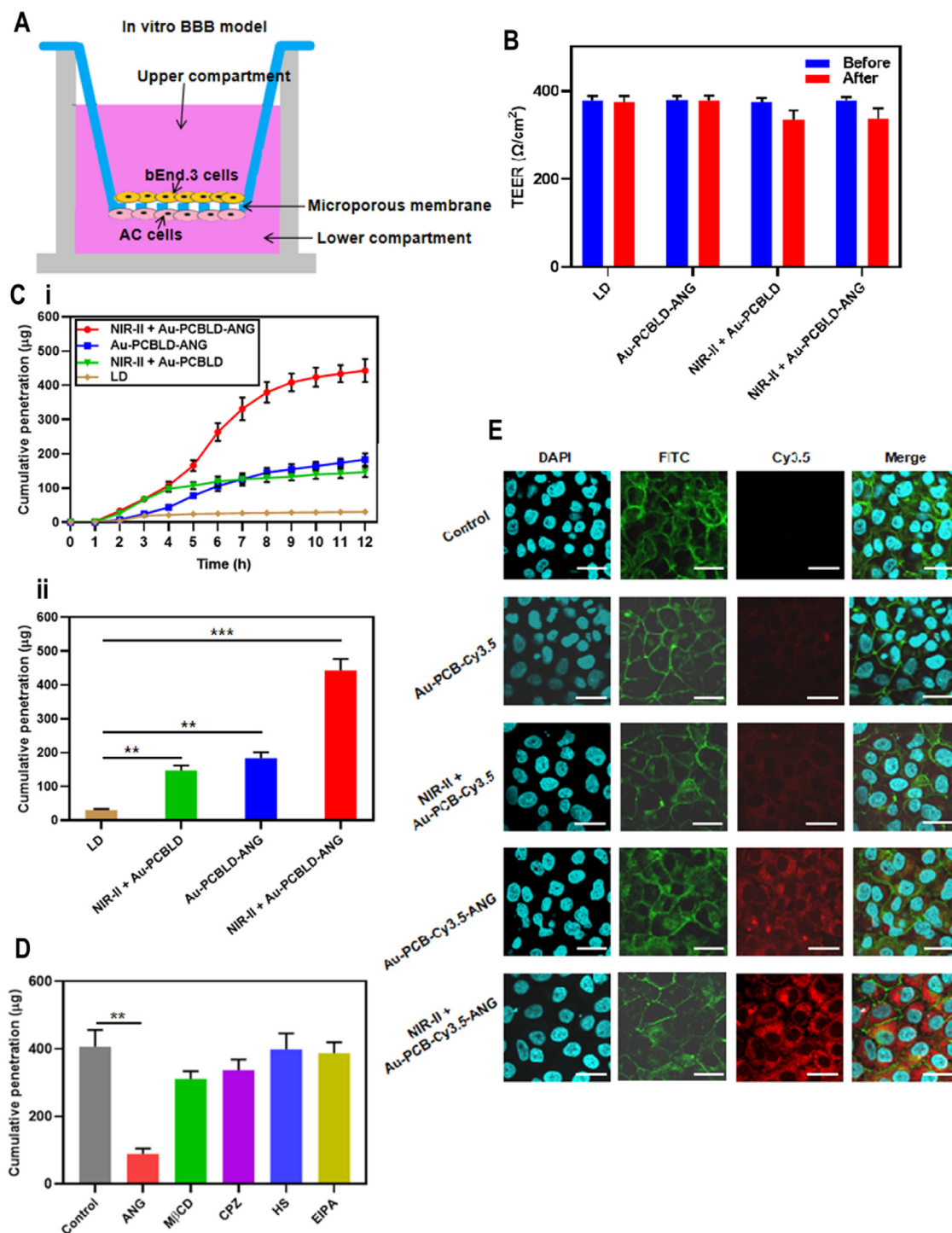
Fig. 3 – Assessment of nanoparticle BBB penetration abilities. (A) Schematic representation of the *in vitro* BBB Transwell system employed to evaluate nanoparticle penetration capabilities. (B) Measurement of TEER before and after transport. (C) BBB penetration abilities of free LD, NIR-II+Au-PCBLD, Au-PCBLD-ANG, and NIR-II+Au-PCBLD-ANG methods. The metric used was the amount of LD released into the receiving solution. (i) Permeation curves of LD through different administration methods. (ii) 24-h permeation amounts of LD through different administration methods. **$P < 0.01$, ***$P < 0.001$. (D) BBB permeation amounts of LD in different groups after treatment with various phagocytosis inhibitors. (DS: dextran sulfate; MβCD: methyl-β-cyclodextrin; CPZ: chlorpromazine; HS: hypertonic sucrose; EIPA: 5-(N-ethyl-N-isopropyl)-amiloride). **$P < 0.01$. (E) Confocal fluorescence imaging illustrating the ability of Cy3.5-labeled NPs to enter bEnd.3 cells. The intercellular tight junction protein occludin is labeled with FITC-antibodies to simulate the BBB. DAPI is shown in blue, FITC is shown in green, and Cy3.5 is shown in red. Scale bar: 20 μm; $n = 3$.

model. Subsequently, we examined the ability of the drug NP to traverse the BBB.

Since peripheral decarboxylases primarily influence the LD drug during administration in this study, we introduced decarboxylase and coenzyme vitamin B6 into the Transwell model to simulate the BBB model system comprehensively. We introduced each type of NP into the upper chamber and collected solutions from the lower chamber at different intervals. Subsequently, these solutions react with sufficient H_2O_2, enabling us to measure the cumulative transmittance of LD in each group and calculate the cumulative transmittance rate within 24 h (Fig. 3C). In the group where free LD was administered alone, only 5.08 % ± 0.51 % could pass through, which was attributed to the presence of decarboxylases. NIR-II irradiation with Au-PCB treatment increased the BBB transmittance to 24.43 % ± 2.52 %, demonstrating the enhancement of BBB permeability through the photothermal effect of NIR-II gold nanorods. In the group with ANG protein but without laser irradiation (Au-PCBLD-ANG), the efficiency of LD passing through the BBB was 30.49 % ± 3.09 %, indicating that ANG protein-mediated endocytosis enhanced drug BBB transmittance. When NIR-II irradiation and ANG were combined in the NIR-II+Au-PCBLD-ANG group, LD transmittance reached 73.86 % ± 5.67 %. It was observed that the concurrent use of NIR-II laser irradiation and ANG-mediated endocytosis significantly increased drug BBB transmittance compared to their application, demonstrating a synergistic promotion. When combined, this enhancement was attributed to the photothermal effect of gold nanorods accelerating ANG endocytosis.

We explored the endocytosis mechanism of these NPs in traversing the BBB. Employing ANG and various endocytosis inhibitors [31], we assessed the inhibitory effects of these inhibitors on LD permeation. Remarkably, the group treated with ANG exhibited a substantial decrease in the ability of NPs to cross the BBB. In contrast, other inhibitors led to varying degrees of reduction in nanoparticle BBB permeation (Fig. 3D). The ANG treatment led to competitive binding, effectively preventing the attachment of the NPs and inhibiting endocytosis. Subsequent treatment with ANG significantly reduced the ability of Au-PCB-ANG NPs to penetrate BBB model cells. This indicates that these NPs primarily cross the BBB through ANG-mediated endocytosis, a mechanism crucial for facilitating the delivery of LD NPs across the BBB.

We utilized fluorescence imaging to evaluate the ability of these NPs to penetrate BBB model cells. PCB-Cy3.5 was synthesized by incorporating the Cy3.5-NH$_2$ fluorescent dye into PCB, replacing PCB-Se-Se-LD (Figs. S1 & S6). This labeled compound was then assembled into Au-PCBCy3.5-ANG NPs. The resulting NPs, labeled with Cys3.5, were cultured with bEnd.3 cells in a BBB model and fluorescence imaging was performed. As depicted in Fig. 3E, the Au-PCBCy3.5 and NIR-II+Au-PCBCy3.5-treated groups exhibited red fluorescence from Cy3.5, indicating that a fraction of NPs entered the cells compared to the control group. However, the groups containing ANG protein, namely Au-PCBCy3.5-ANG and NIR-II+Au-PCBCy3.5-ANG, displayed significantly enhanced fluorescence in the cells. This observation suggests that ANG protein substantially augmented the ability of

NPs to enter bEnd.3 cells, and the NIR-II laser irradiation-induced photothermal effect further facilitated this process. The combined application of photothermal effects and endocytosis significantly enhances drug delivery efficiency across the BBB, highlighting the promising clinical translation potential of these findings. This breakthrough has the potential to advance the development of more effective treatments for various diseases, especially those impacting the central nervous system, where successful BBB penetration is critical.

In summary, the NIR-II AuNR interaction induces a photothermal effect, and simultaneously, endocytosis mediated by the ANG protein enhances BBB permeability. Notably, the photothermal effect actively supports the endocytosis process. The simultaneous activation of these dual mechanisms generates a synergistic effect, effectively enhancing the trans-BBB functionality of drugs.

3.4. Capability of microenvironment regulation and neuroprotective effects

The metabolism of LD itself and the disturbance of thiol homeostasis can initiate a detrimental cycle characterized by increased ROS levels, mitochondrial dysfunction, and reduced reductase enzyme activity [12,13] (Fig. 4A). Our approach aims to break this harmful cycle by reducing ROS levels to alleviate neuro damage. *In vitro*, we examined the environmental regulatory capacity and neuroprotective effects of NIR-II+Au-PCBLD-ANG. To investigate this, we employed human neuroblastoma cells (SH-SY5Y) in our study, chosen for their origin from a human neuroblastoma cell line, which renders them highly similar to human neural cells. These cells exhibit pluripotent differentiation, making them an excellent model for studying neural cells and neurological disorders. Moreover, their high sensitivity to both neuroprotective effects and neurotoxicity makes them particularly suitable for assessing the impacts of neuroprotective agents and potential neurotoxic substances [32]. Initially, we assessed the cytotoxicity of Au-PCBLD-ANG on RA, bEnd3, and SH-SY5Y cells, revealing no significant decrease in cell viability (Fig. 4B). This result suggests that these NPs exhibit low cytotoxicity and do not induce any additional toxicity during treatment in neuronal cell models. To assess the ROS scavenging ability of these NPs, we induced oxidative stress in SH-SY5Y cells by treating them with 5-methyl-1-phenylpyridinium (MPP$^+$). Results indicated that, compared to normal cells, ROS levels in MPP$^+$-treated cells increased by 2.75 ± 0.12-fold, and after treatment with Au-PCBLD-ANG, ROS levels remained at 2.88 ± 0.14-fold (Fig. 4C). This suggests that Au-PCBLD-ANG does not effectively regulate neuronal ROS balance and results in a certain degree of oxidative stress. However, treatment with Au-PCBLD-ANG+NIR-II (5, 10 and 15 μM) could dose-dependently restore ROS levels to 1.96 ± 0.21, 1.52 ± 0.11, and 0.99 ± 0.06 times, respectively. Considering the potential off-target effects of diselenide bonds, they may interact with other antioxidants in cells and participate in protein conformation and function [33]. The interaction with antioxidants can reduce oxidative damage, aligning with our objectives. Results from ROS detection demonstrate that this method effectively reduces ROS levels in cells treated
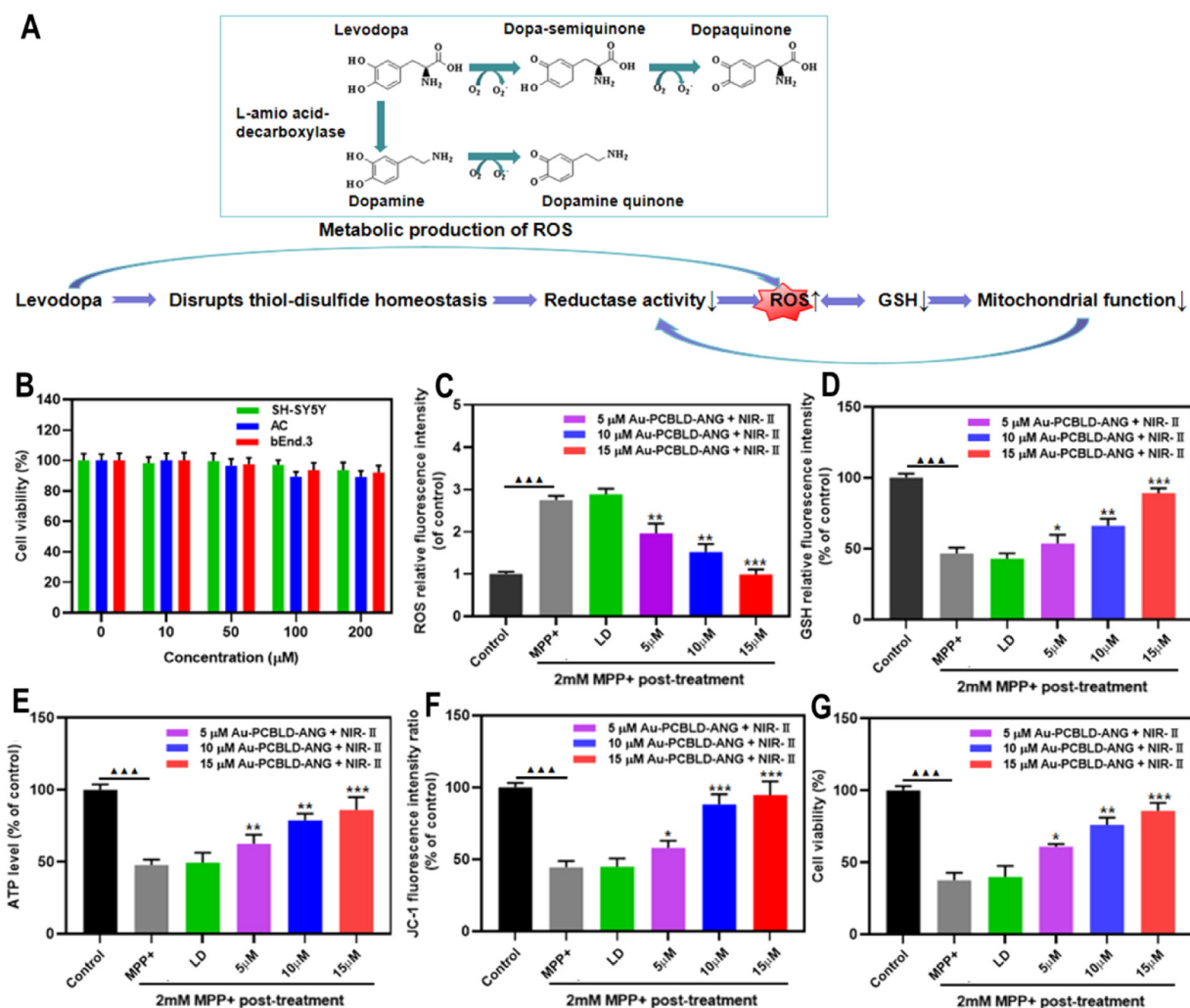
Fig. 4 – NIR-II+Au-PCBLD-ANG treatment alleviates neuronal oxidative stress and reduces neurodamage. (A) Regulatory pathways in the neuronal microenvironment. LD exacerbates oxidative stress through two pathways: disrupting thiol homeostasis and generating ROS during metabolism (resulting in increased ROS levels and decreased GSH levels), creating a vicious cycle between mitochondrial function and oxidative stress, thereby increasing neurotoxicity. Our treatment interrupts this vicious cycle by reducing ROS levels, achieving neuroprotection. (B) Cell viability assessed by CCK-8 assay to evaluate the cytotoxicity of NPs. (C) ROS levels in cells treated with MPP$^+$ and subsequently treated with free LD or different concentrations of NPs. (D) GSH levels in cells treated with MPP$^+$ and subsequently treated with free LD or different concentrations of NPs. (E) ATP levels characterizing mitochondrial function. (F) Mitochondrial membrane potential. (G) Effects of various treatments on neuronal cell viability. NIR-II+Au-PCBLD-ANG treatment significantly alleviates neuro damage caused by MPP$^+$ treatment. $n = 3$. ▲▲▲$P < 0.001$ compared to the control group. *$P < 0.05$, **$P < 0.01$ and ***$P < 0.001$ compared to the MPP$^+$ treatment group.

with MPTP, confirming its robust ROS scavenging capability and that it does not produce significant off-target effects. This suggests that the method can regulate neuronal ROS homeostasis. Similar results were obtained when measuring the oxidative stress marker GSH. Fig. 4D illustrates that this treatment method effectively alleviated the reduction of GSH induced by neuronal oxidative stress in a concentration-dependent manner. The NPs reduced ROS content in neurons, thereby mitigating GSH dimerization [34] and effectively restoring GSH levels.

Studies have indicated that excessive ROS can damage mitochondria and decrease mitochondrial membrane

potential (MMP) [35]. Therefore, we investigated the mitochondrial protective ability of this method by measuring intracellular ATP levels and MMP. The results demonstrated that the combination of Au-PCBLD-ANG treatment (5, 10 and 15 μM) followed by NIR-II laser irradiation could dose-dependently reduce the energy loss induced by MPP$^+$, increasing ATP levels from 47.69 % ± 1.85 % to 62.41 % ± 2.19 %, 78.60 % ± 1.72 %, and 85.88 % ± 2.91 % (Fig. 4E). Membrane potential measurements further confirmed that the method regulated the cellular microenvironment, leading to a dose-dependent increase in membrane potential from 44.46 % ± 4.41 % to 57.95 % ± 5.06 %, 88.14 % ± 6.99 %,
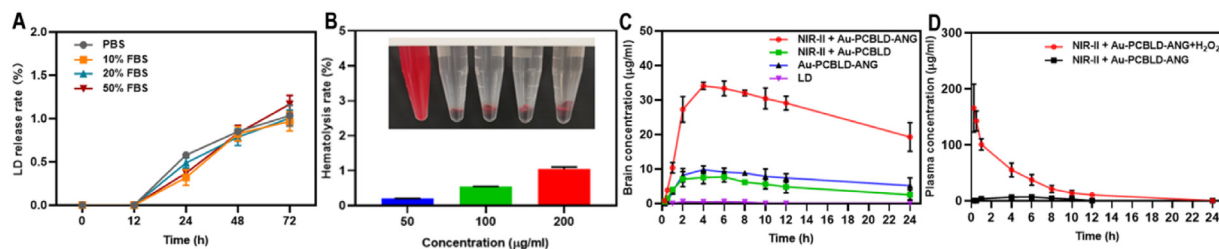
Fig. 5 – Biological safety and pharmacokinetics. (A) LD release measured at different time points. NPs were incubated at 37 °C in PBS with varying concentrations (0, 10 %, 20 %, 50 %) of FBS. (B) Hemolysis assessment of Au-PCBLD-ANG at concentrations of 50, 100 and 200 μg/ml. Water was the positive control, while PBS was the negative control. (C) Brain concentration-time curves in rats exposed to diverse treatments, including free LD, NIR-II+Au-PCBLD, Au-PCBLD-ANG and NIR-II+Au-PCBLD-ANG (laser irradiation at 0.8 W/cm^2, controlled temperature at 41 ± 1 °C, 10 min). (D) LD concentration-time curves in mouse plasma after treatment with NIR-II+Au-PCBLD-ANG, highlighted in black; LD concentration in plasma after adding H$_2$O$_2$ and esterase treatment, depicted in red. n = 3.

and 94.64 % ± 9.43 % (Fig. 4F), demonstrating excellent mitochondrial protection.

We further investigated whether the environmental regulation achieved by this method could confer neuronal protection. When cells were treated with MPP$^+$ to induce neurotoxic damage [36], their activity decreased to 37.55 % ± 5.13 % compared to normal cells. After free LD treatment, cell activity was 39.95 % ± 7.01 % (Fig. 4G), indicating no significant improvement in neuronal toxicity caused by MPP$^+$. However, when cells were treated with Au-PCBLD-ANG (5, 10, and 15 μM) and then irradiated with a 1064 nm laser, their activity significantly increased in a dose-dependent manner (60.91 % ± 1.81 %, 76.02 % ± 5.01 %, and 85.71 % ± 5.60 %; Fig. 4G). Therefore, this administration method demonstrates excellent neuroprotective effects. These findings indicate that this method can regulate the microenvironment and exhibit concentration-dependent neuroprotective effects.

These research findings indicate that this method has the ability to regulate the microenvironment and has neuroprotective effects, and these protective effects are concentration-dependent.

3.5. Biocompatibility and pharmacokinetic studies

Before administering in vivo, we first evaluated the suitability of NPs for intravenous drug delivery. Given that biological variability might affect the stability of diselenide bonds, premature bond cleavage could result in off-target drug release, reducing therapeutic effectiveness and increasing the risk of side effects. To address this concern, we performed serum stability tests on the NPs to confirm their integrity in a biological setting. The drug release rates of Au-PCBLD-ANG within 72 h in PBS, 10 % FBS, 20 % FBS, and 50 % FBS were only 1.09 % ± 0.09 %, 1.04 % ± 0.11 %, 1.10 % ± 0.09 % and 1.17 % ± 0.12 %, respectively, indicating that Au-PCBLD-ANG exhibits ideal stability in serum (Fig. 5A). This nanocarrier demonstrates controlled drug release, minimizing random release into the bloodstream. Considering the potential impact of nanoparticle aggregation on both behavior and therapeutic efficacy in vivo, we incubated Au-PCB-ANG NPs in serum for 72 h to assess their stability. We monitored

their PDI and found it to be 0.23 ± 0.06 after the incubation, which is consistent with their initial PDI. This result suggests that the NPs maintain their dispersion and are unlikely to aggregate while circulating in the bloodstream (Table S1). A hemolysis test of Au-PCBLD-ANG showed no significant hemolytic activity (<5 %) (Fig. 5B), affirming that the Au-PCBLD-ANG formulation does not cause considerable hemolysis and is well-suited for intravenous drug delivery. Given the risk that repeated administration could lead to nanoparticle accumulation in organs, potentially causing toxic reactions and impairing liver and kidney function, we assessed the toxicity of this administration method. We performed immunostaining of the heart, liver, spleen, lungs, and kidneys and conducted biochemical tests to evaluate liver and kidney function. Immunostaining revealed no significant differences in the heart, liver, spleen, lungs, and kidneys before and after administration (Fig. S8). Additionally, serum biochemical indicators of liver and kidney function demonstrated that the nanocarrier exhibited no issues (Table S2). The potential for systemic immune response triggered by NPs is a significant concern, as they might activate, proliferate, and migrate immune cells, leading to systemic inflammation. To evaluate the risk, we measured inflammatory factors and performed routine blood tests following treatment with this method. The results showed no significant differences in the levels of inflammatory markers TNF-α, IL-6 and IL-1β, between the treatment group and the control group (Fig. S9). Additionally, the blood test indicates that the white blood cell count falls within the normal range (Table S3). These findings suggest that this administration method does not induce significant systemic inflammatory responses.

Building on the above-indicated studies, we conducted pharmacokinetic analysis through intravenous injection to comprehend the effectiveness of LD delivery to the brains of treated animals after Au-PCBLD-ANG administration. Pharmacokinetic analysis was performed after administering LD, Au-PCBLD-ANG, NIR-II+Au, and NIR-II+Au-PCBLD-ANG (each group receiving an equivalent of 60 mg/ kg LD). In the brain pharmacokinetic study (Fig. 5C & Table 1), the group injected with free LD showed a peak brain plasma concentration of just 0.54 ± 0.19 μg/ml. In contrast, the

Table 1 – Pharmacokinetic parameters and results in the brain.

	NIR-II+Au-PCBLD-ANG	NIR-II+Au-PCBLD	Au-PCBLD-ANG	LD
C_{max} (µg/ml)	34.09 ± 1.25***	7.64 ± 1.81**	9.80 ± 1.06***	0.54 ± 0.23
T_{max} (h)	4	4	4	2
$T_{1/2}$ (h)	21.70 ± 7.16*	16.85 ± 4.98*	23.74 ± 7.78*	3.92 ± 0.61

C_{max}: peak concentration; T_{max}: time to peak; $T_{1/2}$: half-life. *$P < 0.05$, **$P < 0.01$, and ***$P < 0.001$ compared to the LD group.

NIR-II+Au-PCBLD-ANG group, which utilized both NIR-II laser irradiation and ANG-mediated endocytosis, achieved a much higher peak concentration (C_{max}) of 34.09 ± 1.25 µg/ml. This represents a significant increase in brain drug concentration compared to the injection of free LD. These findings indicate that the combination of ANG targeting the BBB and NIR-II laser irradiation can augment drug permeability across the BBB, resulting in increased LD accumulation in the brain. The half-life ($t_{1/2}$) of the drug in the brain was significantly extended following administration with this method. We attribute this prolongation to the slow release of the drug. Regarding the pharmacokinetic study in the blood of the NIR-II+Au-PCBLD-ANG group (Fig. 5D), minimal free LD was directly detectable at various time points after intravenous blood collection. However, upon adding H_2O_2 to the blood samples and subsequently measuring LD, a substantial amount of LD was observed, with the LD content gradually decreasing over increasing administration time. This suggests that only a minimal amount of the drug is released into the bloodstream following the injection of this drug-loaded nanoparticle. The majority of the drug is released after entering the brain. However, once released into the brain, it does not extensively circulate in the systemic bloodstream. This is attributed to the fact that LD, once released in the brain, would need to traverse the BBB to re-enter the bloodstream. This process is influenced by peripheral brain decarboxylase, resulting in the breakdown and metabolism of LD, preventing it from re-entering the systemic circulation in large quantities. In summary, this method accomplishes targeted and sustained drug release, avoiding pulsatile drug administration.

3.6. Mechanism of NIR-II AuNRs photothermal effect resulting in enhanced BBB permeability

We aimed to assess the efficacy of the NIR-II+Au-PCBLD-ANG formulation in enhancing BBB permeability. Initially, we employed Evans Blue as a tracer to monitor changes in BBB permeability [37]. Mice were injected with NPs and allowed to circulate for 30 min, followed by laser irradiation and the subsequent injection of Evans Blue dye. Then, brain tissue was collected after perfusion through the heart for Evans Blue content measurement (Fig. 6A). Compared to the control group, there was no significant increase in Evans Blue content in the brains of mice following NIR-II laser irradiation with the injection of PBS or PCBLD-ANG alone. This suggests that short-term NIR-II laser irradiation or using ANG protein alone does not induce BBB opening. However, when mice injected with Au-PCBLD or Au-PCBLD-ANG underwent NIR-II irradiation, the Evans Blue content in the mouse brain significantly increased by 8.09 ± 0.56 and $8.33 \pm 0.0.51$ times compared to the control group. This implies that the opening of the BBB results from the photothermal effect of AuNR after NIR-II irradiation. Notably, the Evans Blue content in these two groups did not significantly differ, indicating that the BBB opening is not associated with ANG protein. Additionally, after irradiation, when Evans Blue was injected at different times, we observed a gradual closure of the BBB, fully recovering within 24 h (Fig. 6A). This suggests that the BBB opening induced by the photothermal effect of NIR-II gold nanorods is reversible.

Regarding the mechanisms behind the increased BBB permeability induced by the NIR-II+Au-PCBLD-ANG formulation, our initial consideration was the possibility of brain dehydration or alterations in BBB cell morphology caused by increased temperature. Brain water content detection in mice revealed no significant change after treatment with this method (Fig. 6B). We also conducted BBB permeability studies using lanthanum nitrate as a tracer [38], and the TEM results are shown in Fig. 6C. Compared to the control group, the utilization of this method did not show apparent deformations in the cell morphology of the BBB. However, there was a clear injection of lanthanum nitrate between the cells, with a width of approximately 26 nm. This indicates that this method enhances BBB permeability by opening the tight junctions between cells. Tight junction proteins and adhesion junction proteins primarily mediate tight junctions between BBB cells. We assessed changes in tight junction proteins and adhesion junction proteins before and after treatment, using ZO-1 (zonula occluden-1, a representative tight junction protein), Occludin (a protein that hinders the passage of large molecules), and VCAM (Vascular Cell Adhesion Molecule) as examples [39]. The results indicated that, compared to before treatment, the ZO-1 protein content decreased by 73.42 % $\pm$ 4.78 % after NIR-II+Au-PCBLD-ANG treatment, and the occludin protein content decreased by 82.11 % $\pm$ 8.31 %, with no significant change in the content of the adhesion junction protein (Fig. 6D-6F). Therefore, we conclude that the opening of the BBB may be attributed to a decrease in the content of tight junction proteins induced by this method, leading to the relaxation of tight junctions between BBB cells. Regarding the mechanism responsible for the reduction in tight junction protein levels, one study suggests that it is mediated by the extracellular signal-regulated kinases 1 and 2 (ERK1/2) mitogen-activated protein kinase in response to the downregulation of tight junction proteins induced by heat stress [40]. This study was performed in vitro with intestinal epithelial cells and involved extended exposure
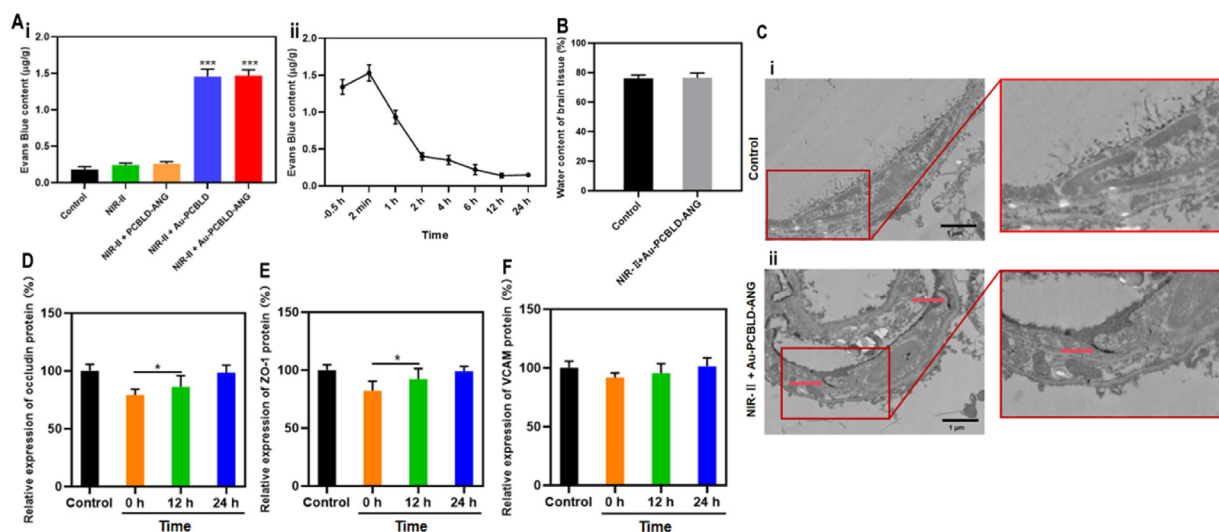
Fig. 6 – Mechanisms of enhanced BBB permeability. (A) BBB permeability revealed by Evans Blue dye. (i) Evans blue content in the brain homogenates after intracardiac perfusion with Evans blue dye following different treatments. (ii) Measurements of Evans Blue content in brain homogenates at different time points following NIR-II+Au-PCBLD-ANG treatment, with intracardiac perfusion of Evans Blue dye. (B) Comparative analysis of brain water content in mice before and after treatment. (C) TEM imaging of the Mouse BBB. (i) TEM imaging of the brain in untreated mice after lanthanum nitrate perfusion (control group) (scale bar: 1 µm). (ii) TEM imaging of the mouse BBB after injection of Au-PCBLD-ANG followed by lanthanum nitrate perfusion (scale bar: 1 µm). (D-F) Quantification of tight junction proteins and adhesion molecules in mouse brain homogenate using ELISA.(D) The relative expression of occludin protein. (E) The relative expression of ZO-1 protein. (F) The relative expression of VCAM protein. $n = 3$. *$P < 0.05$, ***$P < 0.001$.

to heat stress. We will continue to explore the mechanisms behind the reduction of tight junction proteins using this method. Notably, this method causes a reversible opening of the BBB, prompting us to investigate whether repeated administrations affect the BBB's tight junction proteins. Using occludin protein as an example, after a week of continuous treatment followed by a 24-h recovery period, the occludin content reached 98.35 % ± 8.36 % of its pre-treatment level. (Fig. S10), indicating no significant difference. This suggests that the treatment did not affect the reversible restoration of BBB tight junction proteins during this period. Future studies would consider longer-term treatments on the BBB's reversibility and the impact of this reversible restoration on repeated administrations.

3.7. In vivo neuroprotective effects

We conducted pharmacological assessments to evaluate the neuroprotective effectiveness of Au-PCBLD-ANG formulations in a mouse model of PD. The MPTP-induced PD model was employed in our study (Fig. 7A), reflecting key features observed in PD patients, such as reduced brain DA levels, reduced counts of TH+ neurons, and motor impairments [41]. To assess the coordination and activity of our PD model mice, we employed the rotarod, pole climbing, and open field tests [42]. In the rotarod experiment, the PD model group exhibited reduced latency to fall after MPTP treatment, indicating significant impairment in coordination and balance (Fig. 7B). Free LD treatment did not markedly improve coordination and balance due to the influence of peripheral decarboxylase activity, leading to the breakdown

of LD into dopamine, which struggles to cross the BBB. However, LD treatment and a decarboxylase inhibitor (LD and LBH) effectively enhanced motor coordination. The Au-PCBLD-ANG group without laser irradiation and the NIR-II+Au-PCB group without ANG protein showed some improvement in coordination. The Au-PCBLD-ANG group with laser irradiation exhibited the most substantial behavioral improvement. Consistent with these findings, all treatment methods significantly reduced the turnaround time (T-turn) and the total time required to descend the pole (T-total) in the pole test compared to the PD model mice (Fig. 7C). The combination of ANG and laser irradiation demonstrated the most effective motor therapeutic effect. Using an open-field test, we further assessed these mice's exploratory and spontaneous movements. Mice treated with MPTP exhibited significantly reduced spontaneous activity and exploration, challenges overcome by all tested therapeutic methods except for free LD treatment. Within the same duration (5 min), these treatments increased the distance traveled by the mice during free activity (Fig. 7D). Importantly, Au-PCBLD-ANG, in combination with NIR-II irradiation, showed the maximum restoration of motor function in these PD model mice, evidenced by the fewest falls, the longest fall latency, the shortest T-turn, the shortest T-total, and the longest distance traveled. Therefore, the combination of Au-PCBLD-ANG and NIR-II irradiation effectively corrects the motor deficits observed in MPTP-induced injured mice.

Due to the pivotal role of dopamine in controlling balance ability, we assessed the levels of DA and its related metabolites, 3,4-dihydroxyphenylacetic acid (DOPAC) and homovanillic acid (HVA), in brain tissue homogenates [43].
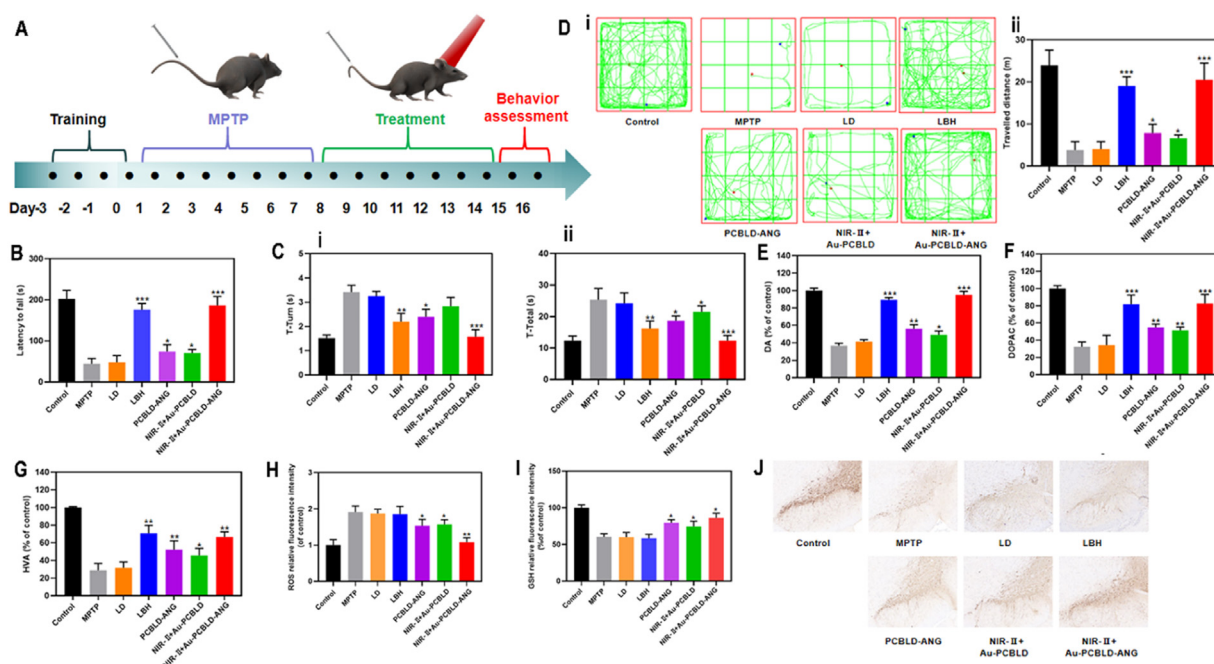
Fig. 7 – Motor behaviours of MPTP-induced PD mice following various treatments. (A) Design of the pharmacological study. (B-D) Effect of different methods, including free LD, LBH (benzydamine), PCBLD-ANG, Au-PCBLD, NIR-II+Au-PCBLD-ANG, on behavioral deficits in MPTP-injected PD mouse models: (B) rotarod test, (C) pole test (i: turnaround time; ii: total time required to descend the pole), and (D) open field test (i: free movement trajectories of mice in the open field arena (green); ii: total distances traveled by mice in different treatment groups). (E-G) Measurement of DA and its metabolites before and after treatment: (E) relative levels of DA, (F) relative levels of DOPAC, and (G) relative levels of HVA. (H) ROS levels in brain homogenates of mice after MPTP and various treatments. (I) GSH levels in brain homogenates of different treatment groups. (J) TH$^+$ staining in the substantia nigra of mice after different treatments. $n = 6$. Compared to the MPTP group: *$P < 0.05$, **$P < 0.01$, ***$P < 0.001$.

Consistent with the impact on the balance, the levels of DA, DOPAC, and HVA in mice treated with MPTP were reduced by 36.86 % ± 2.65 %, 32.26 % ± 5.61 %, and 28.7 % ± 7.90 %, respectively, compared to control mice (Fig. 7E-7G). Treatment with LD did not significantly alter these levels, likely due to peripheral decarboxylase activity limiting its effective penetration into the brain without protective measures. In contrast, Au-PCBLD-ANG treatment without subsequent irradiation restored these levels to 56.20 % ± 4.52 %, 54.88 % ± 3.83 %, and 52.16 % ± 9.98 % in the control group. The NIR-II+Au-PCB group without ANG restored these levels to 49.30 % ± 4.19 %, 51.51 % ± 3.72 %, and 45.67 % ± 8.04 % in the control group. The combination of Au-PCBLD-ANG injection and NIR-II irradiation significantly outperformed the other two methods, increasing these levels to 95.04 % ± 4.11 %, 82.55 % ± 10.58 %, and 66.60 % ± 5.82 % of the control group. This suggests that the synergistic effect of NIR-II laser irradiation-induced photothermal effect and ANG-mediated targeted phagocytosis effectively rectifies the reduced levels of DA, DOPAC and HVA induced by MPTP.

To further explore the therapeutic mechanisms of the NPs, we utilized ELISA to quantify ROS levels in the substantia nigra of mice (Fig. 7H). Following MPTP treatment, brain ROS levels in mice increased to 1.91 ± 0.17 times that of normal mice. Treatment with LD and LBH failed to reduce ROS levels in the brains of Parkinsonian mice effectively. In contrast, the

three treatment methods involving PCBLD reduced brain ROS levels to 1.27 ± 0.07, 1.30 ± 0.12, and 1.07 ± 0.06 times that of normal mice. Remarkably, the NIR-II+Au-PCBLD-ANG group successfully restored ROS levels to normal. Similar outcomes were observed in the assessment of GSH levels (Fig. 7I), where the NIR-II+Au-PCBLD-ANG group exhibited the most robust GSH restoration, elevating GSH levels from 60.32 % ± 4.31 % to 86.10 % ± 6.33 % relative to the MPTP-treated group. We also evaluated the ability of Au-PCBLD-ANG formulations to prevent MPTP-induced damage to dopaminergic neurons in the substantia nigra. Through immunohistochemical staining to detect TH$^+$ neurons in treated mice (Fig. 7J), we found that LD treatment alone did not enhance the number of TH$^+$ neurons in the substantia nigra. However, all groups involving ROS-responsive LD delivery were able to mitigate TH$^+$ neuronal damage, with the combination of ANG and NIR-II achieving the most effective protection of TH$^+$ neurons. This indicates that injecting Au-PCBLD-ANG and NIR-II irradiation sufficiently reduces the loss of TH$^+$ neurons in these PD model mice.

In summary, the significant accumulation of LD and its metabolites in the brain, coupled with the reduced oxidative stress levels, suggests that this administration method can more effectively accomplish dopamine supplementation and enhance the microenvironment in the brains of Parkinsonian mice. In addition to achieving high brain delivery, this

administration method does not cause significant tissue damage or systemic inflammatory responses. This highlights its potential for clinical development and applicability in treating other brain diseases.

4.   Conclusion

This investigation has successfully developed a nanotherapeutic system utilizing a NIR-II, AuNRs and ANG, facilitating efficient traversal of the BBB and controlled release of LD in response to ROS. This innovative design provides substantial advancements in LD therapy by addressing two key challenges. Firstly, the BBB-targeting property of ANG enhances nanoparticle accumulation and improves transport efficiency through phagocytosis. NIR-II AuNR's photothermal effect enhances BBB permeability and synergizes phagocytosis, resulting in reversible BBB opening. Secondly, this carrier protects LD from peripheral decarboxylase interference, enabling unhindered passage through the BBB while regulating the local microenvironment. The ROS-responsive release mechanism reduces ROS levels in the central nervous system, safeguarding mitochondria and neurons. Consequently, NIR-II+ Au-PCBLD-ANG significantly improves motor dysfunction and pathological indicators in a mouse model of PD. This drug delivery system, which crosses the BBB, responds to ROS, and leverages photothermal effects and phagocytosis, presents a promising platform for more effective PD therapy with LD, holding great potential for advancements in neurology and PD treatment.

Conflicts of interest

The authors report no conflicts of interest. The authors alone are responsible for the content and writing of this article.

Acknowledgments

Supplementary materials

Supplementary material associated with this article can be found, in the online version, at doi:10.1016/j.ajps.2024.100963. The figures with "S" before the serial number are included in the Supplementary material.

REFERENCES

[1] Bloem BR, Okun MS, Klein C. Parkinson's disease. Lancet 2021;397(10291):2284–303.

[2] Niu X, Chen J, Gao J. Nanocarriers as a powerful vehicle to overcome blood-brain barrier in treating neurodegenerative diseases: focus on recent advances. Asian J Pharm Sci 2019;14(5):480–96.

[3] Poewe W, Seppi K, Tanner CM, Halliday GM, Brundin P, Volkmann J, et al. Parkinson disease. Nat Rev Dis Primers 2017;3(1):17013.

[4] Dias V, Junn E, Mouradian MM. The role of oxidative stress in Parkinson's disease. J Parkinsons Dis 2013;3(4):461–91.

[5] Sepasi T, Ghadiri T, Ebrahimi-Kalan A, Bani F, Talebi M, Rahbarghazi R, et al. CDX-modified chitosan nanoparticles remarkably reduce therapeutic dose of fingolimod in the EAE model of mice. Int J Pharm 2023;636(1):122815.

[6] Zeinali M, Abbaspour-Ravasjani S, Ghorbani M, Babazadeh A, Soltanfam T, Santos AC, et al. Nanovehicles for co-delivery of anticancer agents. Drug Discov Today 2020;25(8):1416–30.

[7] Ballabh P, Braun A, Nedergaard M. The blood-brain barrier: an overview: structure, regulation, and clinical implications. Neurobiol Dis 2004;16(1):1–13.

[8] Li X, Vemireddy V, Cai Q, Xiong H, Kang P, Li X, et al. Reversibly modulating the blood-brain barrier by laser stimulation of molecular-targeted nanoparticles. Nano Lett 2021;21(22):9805–15.

[9] Pardridge WM. Drug transport across the blood-brain barrier. J Cereb Blood Flow Metab 2012;32(11):1959–72.

[10] Connolly BS, Lang AE. Pharmacological treatment of Parkinson disease: a review. JAMA 2014;311(16):1670–83.

[11] Armstrong MJ, Okun MS. Diagnosis and treatment of Parkinson disease: a review. JAMA 2020;323(6):548–60.

[12] Liedhegner EA, Steller KM, Mieyal JJ. Levodopa activates apoptosis signaling kinase 1 (ASK1) and promotes apoptosis in a neuronal model: implications for the treatment of Parkinson's disease. Chem Res Toxicol 2011;24(10):1644–52.

[13] Muller T, Trommer I, Muhlack S, Mueller BK. Levodopa increases oxidative stress and repulsive guidance molecule A levels: a pilot study in patients with Parkinson's disease. J Neural Transm 2016;123(4):401–6.

[14] Shin JY, Ahn YH, Paik MJ, Park HJ, Sohn YH, Lee PH. Elevated homocysteine by levodopa is detrimental to neurogenesis in parkinsonian model. PLoS One 2012;7(11):e50496.

[15] Muller T, Mohr JD. Long-term management of Parkinson's disease using levodopa combinations. Expert Opin Pharmacother 2018;19(9):1003–11.

[16] Alkilany AM, Thompson LB, Boulos SP, Sisco PN, Murphy CJ. Gold nanorods: their potential for photothermal therapeutics and drug delivery, tempered by the complexity of their biological interactions. Adv Drug Deliv Rev 2012;64(2):190–9.

[17] Habib S, Singh M. Angiopep-2-modified nanoparticles for brain-directed delivery of therapeutics: a review. Polymers 2022;14(4):712.

[18] Zhang J, Jin J, Du Y, Zhou X, Liang H, Jiang W. Enhancing the stability of single-stranded DNA on gold nanoparticles as molecular machines through salt and acid regulation. J Mater Chem B 2019;7(36):5554–62.

[19] Li Y, Cheng Q, Jiang Q, Huang Y, Liu H, Zhao Y, et al. Enhanced endosomal/lysosomal escape by distearoyl phosphoethanolamine-polycarboxybetaine lipid for systemic delivery of siRNA. J Control Release 2014;176(1):104–14.

[20] Sever MJ, Wiker JJ. Synthesis of peptides containing DOPA (3,4-dihydroxyphenylalanine). Tetrahedro 2001;57(29):6139–46.

[21] Wang YN, Wei WT, Yang CW, Huang MH. Seed-mediated growth of ultralong gold nanorods and nanowires with a wide range of length tunability. Langmuir 2013;29(33):10491–7.

[22] Kim KA, Kim D, Kim JH, Shin YJ, Kim ES, Akram M, et al. Autophagy-mediated occludin degradation contributes to blood-brain barrier disruption during ischemia in bEnd.3 brain endothelial cells and rat ischemic stroke models. Fluids Barriers CNS 2020;17(1):21.

[23] Spampinato SF, Merlo S, Fagone E, Fruciano M, Barbagallo C, Kanda T, et al. Astrocytes modify migration of PBMCs induced by beta-amyloid in a blood-brain barrier in vitro model. Front Cell Neurosci 2019;13(1):337.

[24] Goldim M, Della GA, Petronilho F. Using Evans Blue dye to determine blood-brain barrier integrity in rodents. Curr Protoc Immunol 2019;126(1):e83.

[25] Ding GR, Qiu LB, Wang XW, Li KC, Zhou YC, Zhou Y, et al. EMP-induced alterations of tight junction protein expression and disruption of the blood-brain barrier. Toxicol Lett 2010;196(3):154–60.

[26] Dutta D, Kundu M, Mondal S, Roy A, Ruehl S, Hall DA, et al. RANTES-induced invasion of Th17 cells into substantia nigra potentiates dopaminergic cell loss in MPTP mouse model of Parkinson's disease. Neurobiol Dis 2019;132(1):104575.

[27] Deng X, Liang S, Cai X, Huang S, Cheng Z, Shi Y, et al. Yolk-Shell structured Au Nanostar@Metal-Organic framework for synergistic chemo-photothermal therapy in the second near-infrared window. Nano Lett 2019;19(10):6772–80.

[28] Guo B, Feng Z, Hu D, Xu S, Middha E, Pan Y, et al. Precise deciphering of brain vasculatures and microscopic tumors with dual NIR-II fluorescence and photoacoustic imaging. Adv Mater 2019;31(30):e1902504.

[29] Ma N, Li Y, Xu H, Wang Z, Zhang X. Dual redox responsive assemblies formed from diselenide block copolymers. J Am Chem Soc 2010;132(2):442–3.

[30] Modarres HP, Janmaleki M, Novin M, Saliba J, El-Hajj F, RezayatiCharan M, et al. In vitro models and systems for evaluating the dynamics of drug delivery to the healthy and diseased brain. J Control Release 2018;273(1):108–30.

[31] Israel LL, Braubach O, Galstyan A, Chiechi A, Shatalova ES, Grodzinski Z, et al. A combination of tri-leucine and angiopep-2 drives a polyanionic polymalic acid nanodrug platform across the blood-brain barrier. ACS Nano 2019;13(2):1253–71.

[32] Xicoy H, Wieringa B, Martens GJ. The SH-SY5Y cell line in Parkinson's disease research: a systematic review. Mol Neurodegener 2017;12(10):10.

[33] Zhang F, Li X, Wei Y. Selenium and selenoproteins in health. Biomolecules 2023;13(5):7993.

[34] Maiorino M, Conrad M, Ursini F. GPx4, Lipid peroxidation, and cell death: discoveries, rediscoveries, and open issues. Antioxid Redox Signal 2018;29(1):61–74.

[35] Ji W, Li Y, Peng H, Zhao R, Shen J, Wu Y, et al. Self-catalytic small interfering RNA nanocarriers for synergistic treatment of neurodegenerative diseases. Adv Mater 2022;34(1):e2105711.

[36] Isoda K, Nagata R, Hasegawa T, Taira Y, Taira I, Shimizu Y, et al. Hepatotoxicity and drug/chemical interaction toxicity of nanoclay particles in mice. Nanoscale Res Lett 2017;12(1):199.

[37] Li Q, Tang Z, Zhang Y, Yuan T, Yuan B, Du L, et al. Application of low-intensity ultrasound by opening blood-brain barrier for enhanced brain-targeted drug delivery. Int J Pharm 2023;642(1):123191.

[38] de Paula LSL, Kalapothakis E, Da CM. Breakdown of the blood-brain barrier and neuropathological changes induced by Phoneutria nigriventer spider venom. Acta Neuropathol 2003;105(2):125–34.

[39] Peng H, Li Y, Ji W, Zhao R, Lu Z, Shen J, et al. Intranasal administration of self-oriented nanocarriers based on therapeutic exosomes for synergistic treatment of Parkinson's disease. ACS Nano 2022;16(1):869–84.

[40] Yong Y, Li J, Gong D, Yu T, Wu L, Hu C, et al. ERK1/2 mitogen-activated protein kinase mediates downregulation of intestinal tight junction proteins in heat stress-induced IBD model in pig. J Therm Biol 2021;101(1):103103.

[41] Chen T, Liu W, Xiong S, Li D, Fang S, Wu Z, et al. Nanoparticles mediating the sustained puerarin release facilitate improved brain delivery to treat Parkinson's disease. ACS Appl Mater Interfaces 2019;11(48):45276–89.

[42] Sasson E, Anzi S, Bell B, Yakovian O, Zorsky M, Deutsch U, et al. Nano-scale architecture of blood-brain barrier tight-junctions. Elife 2021;10(1):e63253.

[43] Liu Y, Liu W, Xiong S, Luo J, Li Y, Zhao Y, et al. Highly stabilized nanocrystals delivering Ginkgolide B in protecting against the Parkinson's disease. Int J Pharm 2020;577(1):119053.